J Sol-Gel Sci Technol (2016) 79:51–58
DOI 10.1007/s10971-016-4028-x

ORIGINAL PAPER: FUNCTIONAL COATINGS, THIN FILMS AND MEMBRANES (INCLUDING DEPOSITION TECHNIQUES)

Effect of iron doping on the structural and optical properties of CeO_2 films

Duangdao Channei[1,2] · Auppatham Nakaruk[3] · Sukon Phanichphant[4] · Pramod Koshy[5] · Charles Christopher Sorrell[5]

Received: 19 June 2015 / Accepted: 17 March 2016 / Published online: 25 March 2016

Abstract Undoped and Fe-doped CeO_2 thin films were fabricated by spin coating on F-doped tin oxide glass substrates followed by annealing at 500 °C for 15 h. The concentration of the dopant was varied from 2 to 10 % iron by weight (metal basic). Glancing angle X-ray diffraction and laser Raman microspectroscopy indicated that the films consisted only of CeO_2 without any impurity phases of Fe_xO_y. The thickness of the films was determined by dual-beam focused ion beam milling to be ~150 nm for undoped film, while Fe-doped CeO_2 films have thickness of ~200 nm for all dopant samples. The transmission spectra from UV–visible spectrophotometry showed a redshift of the absorption edge of the doped films, and the optical indirect band gap of the films decreased from 3.48 to 3.20 eV with increasing dopant concentration. Furthermore, the results have been proposed in the diagram of electron–hole trapping.

Graphical Abstract

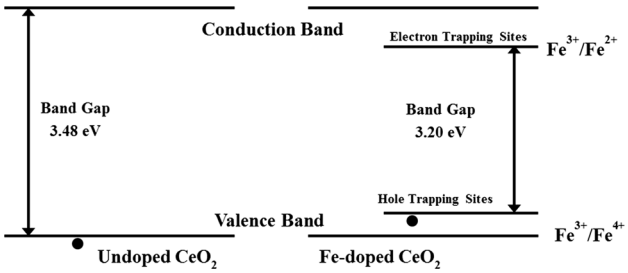

Keywords Cerium dioxide · Spin coating · Thin film · Optical properties · Crystallinity

1 Introduction

CeO_2 has been widely applied in recent years for many applications such as heterogeneous catalysts for automobile exhaust gas emission control [1], catalysts for water purification [2], electrolyte materials for solid oxide fuel cells (SOFC) [3], and thin-film barrier layers [4]. The increased applicability of CeO_2 is due to its excellent physical and chemical properties, such as high oxygen storage capacity (OSC) [5], high optical transparency in the visible region [6], and high refractive index [7]. For photocatalytic processes, it is commonly known that electron–hole pair generation is very essential, and for this purpose, the energy of the incident photon energy has to be at least equal to the band gap of the materials [8, 9]. CeO_2 is a wide-band-gap semiconductor with a band gap of 3.2 eV, and thus, it can only be activated with ultraviolet light (UV light) which comprises only 3–5 % of the complete incident

✉ Duangdao Channei
duangdaoc@nu.ac.th

1 Department of Chemistry, Faculty of Science, Naresuan University, Phitsanulok 65000, Thailand

2 Research Center for Academic Excellence in Petroleum, Petrochemicals and Advanced Materials, Faculty of Science, Naresuan University, Phitsanulok 65000, Thailand

3 Department of Civil Engineering, Faculty of Engineering, Center of Excellence for Innovation and Technology for Water Treatment, Naresuan University, Phitsanulok 65000, Thailand

4 Materials Science Research Center, Faculty of Science, Chiang Mai University, Chiang Mai 50200, Thailand

5 School of Materials Science and Engineering, Faculty of Science, UNSW Australia, Sydney, NSW 2052, Australia

solar spectrum [10]. Therefore, there has been an increasing focus on the development of techniques to enhance the efficiency of the photocatalyst by extending the range of activating wavelengths to the visible region which comprises ~40 % of total solar spectrum [11–13]. Several methods have been used to modify the electronic structure of CeO_2 such as transition metal doping with scandium (Sc) [14], titanium (Ti) [15], manganese (Mn) [16], iron (Fe) [17], cobalt (Co) [18], nickel (Ni) [19], copper (Cu) [20], or zinc (Zn) [21]. Among these, Fe doping is believed to have the most potential to decrease the band gap of CeO_2 and thus to enhance the photocatalytic efficiency since it can enhance the trapping of charge carriers and also inhibit electron–hole recombination during irradiation. Therefore, charge transfer processes can be improved, and this can result in greater photoactivity in the visible region [22–24].

Many fabrication techniques such as pulsed laser deposition (PLD) [25], metal–organic chemical vapor deposition (MOCVD) [26], sputtering [27], reactive DC magnetron sputtering [28], electron beam evaporation [29], spray pyrolysis [30], and sol–gel spin coating methods have been reported for the fabrication of CeO_2 thin films [31]. The latter is one of the most advantageous options due to its simplicity of operation and low cost of material precursors. Moreover, the fabrication of thin films by spin coating technique does not require expensive vacuum conditions. There have been very few publications on the performance of CeO_2 thin films coated on conductive substrates such as F-doped SnO_2 (FTO)-coated glass. There is not much difference in the coated materials on FTO and ITO for photoelectrochemical and photovoltaic applications [32]. However, the price consideration between FTO and ITO makes FTO more advantageous than ITO. Yang et al. [33] reported that the current–voltage photovoltaic performance of dye-sensitized solar cells (DSSCs) using FTO coated with a TiO_2 showed a maximum conversion efficiency of 7.8 %, while bare FTO substrate provided electric energy conversion efficiency of 5.9 %.

This present work focused on the effect of iron doping on the mineralogical, microstructure, compositional, and optical properties of CeO_2 thin films on FTO-coated glass substrates fabricated by spin coating and annealing processes.

2 Experimental

The sol–gel precursor was prepared by dissolving cerium chloride heptahydrate (analytical grade, 99.9 wt% purity, Sigma-Aldrich) in methanol (reagent plus ≥99.9 wt% purity, Sigma-Aldrich) to obtain a solution with 0.5 M Ce concentration. Subsequently, iron (III) chloride hexahydrate (analytical grade, 97 wt% purity, Sigma-Aldrich) was added to the above solution to achieve Fe dopant concentrations of 2, 4, 6, 8, and 10 wt%. Afterward, 0.02 M of citric acid (analytical grade, 99.0 wt% purity, Sigma-Aldrich) was added into the mixed solution in order to prevent cracking and excessive shrinkage of the films [34]. The mixed solution was stirred at 500 rpm for 20 min at room temperature until it became a homogeneous solution. Subsequently, the solution was deposited on FTO-coated glass substrates (Wu-Han Geao Instruments Science and Technology Co., Ltd., China, 5 × 5 × 0.2 cm of dimension) by using a spin coating machine (Laurell WS-65052).

This process involved a total of 10 cycles, each involving the deposition of 0.2 mL of the solution on to the substrate that is spinning at 2000 rpm, followed by drying with an additional spinning for 15 s. A simple schematic of the spin coating process is shown in Fig. 1. The annealing of the deposited films was done in a muffle furnace at 500 °C for 5 h; the heating rate to the top temperature was 5 °C/min, while the cooling was done by natural cooling.

Glancing angle X-ray diffraction (GAXRD, Phillips X'pert Materials Research Diffraction, CuK_α, 45 kV, 40 mA, step size 0.02° 2θ, speed 6°/min 2θ with 1° of set angle) and laser Raman spectroscopy (Renishaw's inVia Raman, He-Cd UV laser excitation source of wavelength 442 nm) were used for the mineralogical characterization of the films. The film thickness was determined using dual-beam focused ion beam (FIB) milling (XT Nova NanoLab 200). The transmission spectrum in the visible region (300–800 nm) was obtained using a dual-beam UV–visible spectrometer (PerkinElmer Lambda 35). The optical indirect band gap was calculated from transmission data using the method of Tauc and Menth [35]. Furthermore, the changes in the valence state of Ce and Fe were determined using thermodynamic stability diagrams calculated using FactSage 6.0 software (Predom mode).

3 Results and discussion

For the undoped and Fe-doped CeO2 films, GAXRD analyses showed that the major phase was CeO_2 which was indexed as a cubic fluorite, matching that of JCPDS 34-03940 [36]. No other peaks from either metallic iron or Fe_xO_y were found in the XRD patterns (see Fig. 2). The XRD data showed that the intensity of the CeO_2 peak in the doped films is lower than that in the undoped film.

However, no significant changes in intensity were observed among the films with varying dopant levels. Nonetheless, it should be noted that the diffraction peak associated with the (200) plane shifted to higher angles with increasing dopant levels.

These data suggest that the Fe dopant has formed a solid solution with the Ce–O lattice. This is further supported by the observed slight decrease in the lattice parameter owing

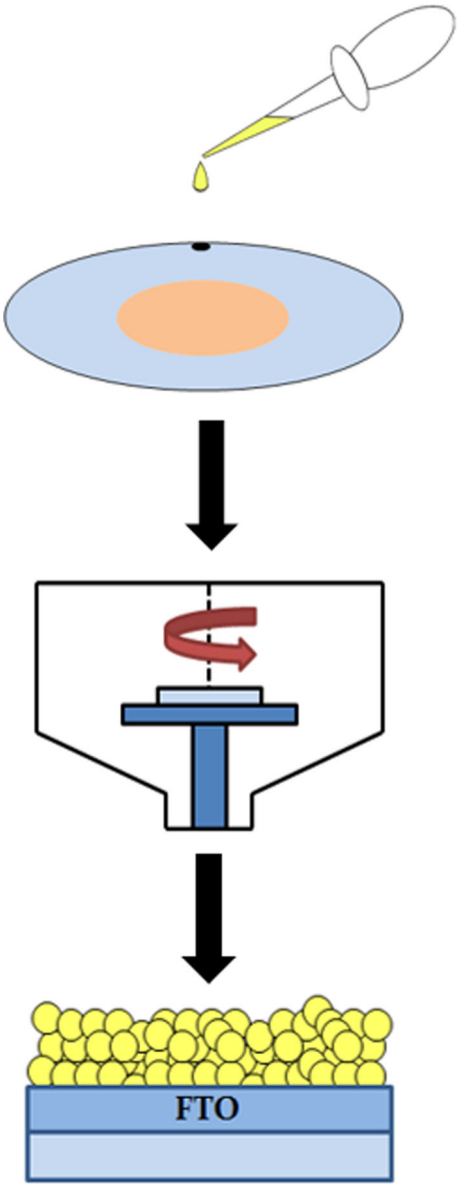

Fig. 1 Sol–gel spin coating process for fabrication CeO_2 or Fe-doped CeO_2 films

to the lattice distortion effects associated with doping with a smaller cation such as Fe^{3+} (Table 1; parameters were calculated using Eqs. 1–3 [37]).

$$d - \text{spcaing} = \frac{1.54}{2\sin\theta} \tag{1}$$

$$\text{Lattice parameter}(a) = \sqrt{\frac{d^2}{h^2 + l^2 + k^2}} \tag{2}$$

$$\text{Unit cell volume} = a^3 \tag{3}$$

where a = lattice parameter (side of cubic cell, $a = b = c$ axis), θ = angle of (200) plane, and (hkl) plane = hkl plane at the selected diffraction peak.

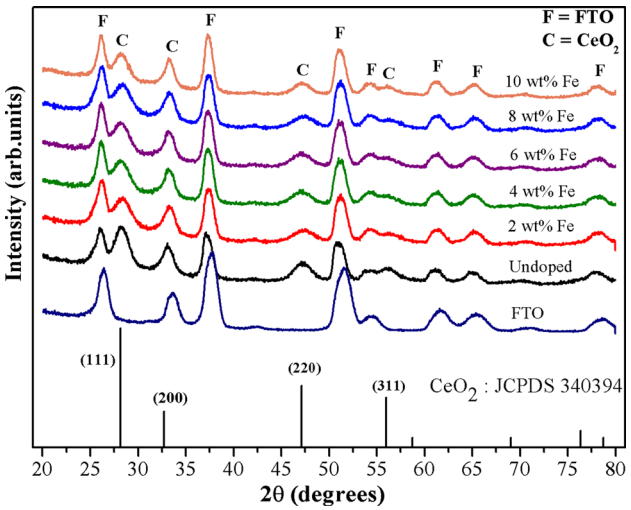

Fig. 2 Glancing angle X-ray diffraction data of undoped and Fe-doped CeO_2 films

The glancing incident X-ray beam has a depth of penetration of ~300 nm [38, 39], and since the CeO_2 thin films are only ~200 nm in thickness, the clear peaks of the FTO substrate are seen in the XRD pattern (see Fig. 2). It is interesting to note that there is also a shift in the FTO peak position (~37° 2θ) compared to the uncoated and unannealed substrate. The effect of contaminant diffusion from the substrate to the film is often overlooked even though it can have a significant impact on the performance of the films. The change in characteristics of the FTO layer is expected to have implications for the optical properties of the coated and annealed films.

This suggests that the heat treatment temperature of 500 °C had an effect on modifying the crystallographic properties of the substrate, and this could be attributed to the diffusion of silicon and sodium cations to diffuse into FTO and also CeO_2 thin film [40]. In addition, tin cation can also diffuse from FTO into CeO_2 thin film. These cation ions (silicon, sodium, and tin) also act as inhibitor to prevent the grain growth, resulting in small crystallite size. The latter also acts to increase the optical band gap.

Laser Raman spectroscopy (see Fig. 3) was used to obtain further information on the mineralogical characteristics of the films since this technique is more sensitive than XRD. The results show that the peak intensity of the major CeO_2 peak decreased significantly with increasing Fe dopant levels, and this suggest that increasing addition of Fe dopant results in amorphization of the films. This also confirms that Fe dopants are potentially present at the grain boundaries and is hindering the recrystallization of CeO_2 at high concentrations, leading to a decline in the intensity of the CeO_2 peak.

The cross-sectional image of Fe-doped CeO_2 and undoped CeO_2 thin films is shown in Fig. 4. The average

Table 1 Calculated *d*-spacing, lattice parameters, and unit cell volume for undoped and Fe-doped CeO_2 thin films

Fe doping concentration (wt%)	200 plane			
	2θ (degree)	*d*-spacing (nm)	Lattice parameter (nm)	Unit cell volume (nm^3)
0	32.99	0.27	0.47	0.10
2	34.21	0.26	0.47	0.10
4	34.27	0.26	0.46	0.10
6	34.33	0.26	0.46	0.10
8	34.46	0.25	0.45	0.09
10	34.62	0.25	0.45	0.09

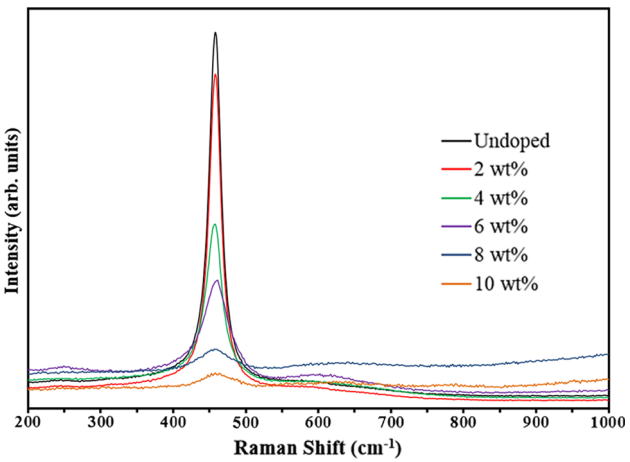

Fig. 3 Raman spectra for undoped and Fe-doped CeO_2 films

thickness of the films was calculated in respect of the vertical (usually at a tilt of 52°) [41]. The undoped CeO_2 film deposited on FTO substrate had a thickness of ~150 nm CeO_2, while Fe-doped CeO_2 films had thicknesses of ~200 nm, irrespective of the dopant content.

Furthermore, the change in film thickness may be correlated with the diffusion of cations from the substrate toward the growing film. For thinner films, the cation ion diffusion from the substrates to the films is much higher than in the thick films, which limits the degree of crystallinity of CeO_2.

However, the effect of the Fe^{3+} cation dopant cannot be neglected. The XRD result suggested that Fe^{3+} cation is a more effective grain growth inhibitor than the cation diffusion from the substrate. Since the degree of crystallinity growth is dependent on grain boundary diffusion, doping with Fe^{3+} cation would inhibit grain growth and decrease the degree of crystallinity of CeO_2 upon increasing the Fe^{3+} dopant content [42].

Thermodynamic stability diagrams were calculated to determine the stability regions for ions of different valences (corresponding oxides) as a function of temperature and pressure (Fig. 5). Consequently, these diagrams are useful in estimating the potential valence states of Ce and Fe species after film processing under certain experimental conditions.

Since the atmospheric pressure is 0.10 MPa (1.00 atm) and air composition is approximately 20 vol% O_2, the oxygen partial pressure (pO_2) of air is ~0.02 MPa (~0.20 atm). The calculated thermodynamic stability diagram of Ce–O and Fe–O under the annealing conditions of 500 °C in air ($\log pO_2 = -0.69$) shows that the cations would be present in the form of Ce^{4+} and Fe^{3+}, respectively.

Based on the thermal stability diagrams, it can be assumed that Fe^{3+} is present in the films. Based on this assumption, it is possible to predict the mechanism of electron−hole trapping in the Fe-doped CeO_2 samples.

Since the crystal radii of Fe^{3+}, Ce^{4+}, and O^{2-} in -sixfold coordination are 0.072, 0.101, and 0.126 nm, respectively [43]; therefore, there are two possible routes for substitution that could occur and the mechanisms involved can be explained further as follows:

- Fe^{3+} ion substitution for Ce^{4+} ion results in the production of a structure with holes in the CeO_2 structure; this results in the creation of electron acceptor levels of Fe^{3+} inside CeO_2 band structure (shallow hole trapping).
- An unlikely possibility is the substitution of O^{2-} ion by Fe^{3+} ion, which results in the formation of an ionic bond. The free electrons of Fe^{3+} (non-bonding one) can function as electron donors by creating a new energy level at the bottom of conduction band of CeO_2 (shallow electron trapping).

However, substitution by metals of ionic radii differing by more than 15 % from that of the parent metal is unlikely to happen. The crystal radii data show that the difference in radii between Ce^{4+} and Fe^{3+} is ~28 %. It is likely that the interstitials of the Ce–O structure would be occupied by the Fe^{3+} ion; in this case, electrons from Fe^{3+} are free to move within the CeO_2 lattice. The creation of electron trapping sites in the CeO_2 band structure (by doping) can serve as electron donors. From the XRD peak shift in Fig. 2, these

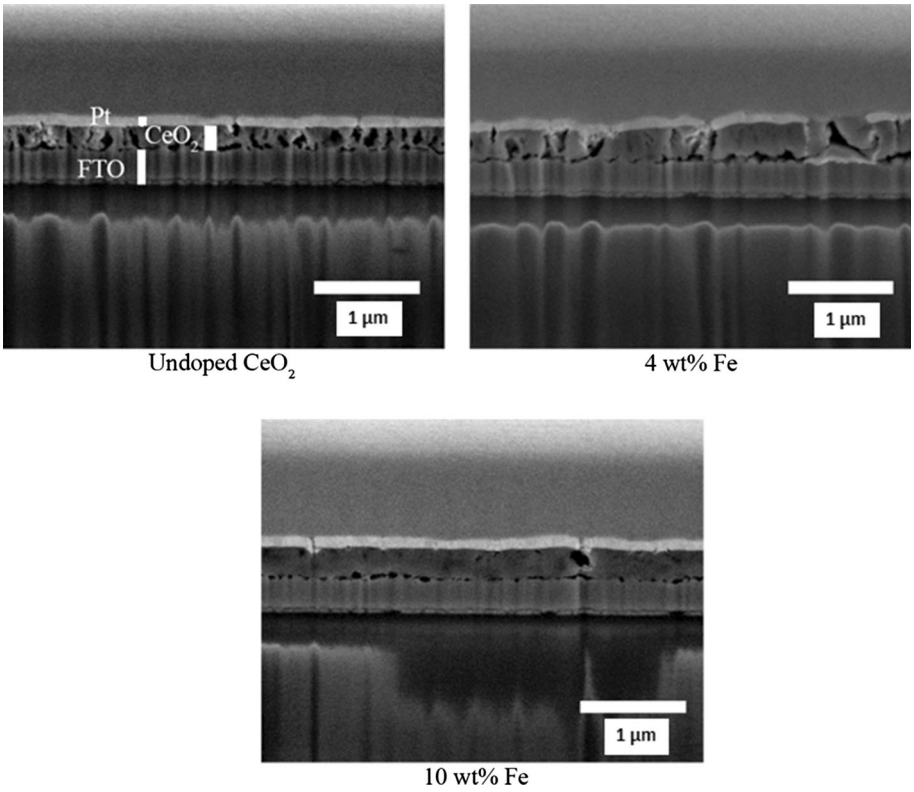

Fig. 4 Cross-sectional images showing the thickness of undoped and Fe-doped CeO_2 thin films on FTO-coated glass substrates

observations could be ascribed to the interstitials of Ce^{4+} ions (0.101 nm) being occupied by Fe^{3+} ions (0.072 nm), as shown in Fig. 6.

The transmission spectra for undoped and Fe-doped CeO_2 thin films were in good agreement and support the possible explanation for interstitial solid solutions. The undoped CeO_2 film showed a high transmittance in the visible range of $\sim$85 %. The extent of transmission decreased significantly with increasing doping levels (see Fig. 7). A possible explanation is that Fe^{3+} is a major factor affecting the reduction yield of effective light transmission. This can be attributed to the formation of an interstitial solid solution of Fe^{3+} within the CeO_2 lattice, resulting in a poorly crystalline structure leading to enhanced scattering of photons [44, 45].

Since CeO_2 is known to be a transparent conductive oxide, undoped CeO_2 thin films are transparent to visible light (400–800 nm). However, Fig. 7 shows that the transmission in the visible region decreased with increasing Fe dopant level since there was a slight increase in the thickness of the films containing dopants although this is not believed to significantly affect the transmission. A significant factor is the color of the films; Fe doping caused a change in color of the films from colorless (transparent) to dark yellow. This would result in absorption of light in the visible range, and resultantly, there would be a lowering of the transmission. Furthermore, doping with Fe was observed to shift the absorption edge toward longer wavelengths. The optical indirect band gap (E_g) of the films calculated using the Tauc method (Fig. 8) showed that optical indirect band gap decreased from 3.48 eV for undoped CeO_2 to 3.20 eV for 10 wt% Fe-doped CeO_2.

Prior studies have been conducted on the deposition of CeO_2 films using different techniques such as spray pyrolysis, sol–gel, magnetron sputtering, electron beam evaporation, and PLD [46–49]. All these studies have shown that the band gap and electronic structure of the films can be modified by Fe doping. However, in the present work, the value of the indirect band gap obtained is lower than those observed in prior work; furthermore, in prior work, the band gaps were observed to increase with increasing doping levels, which is in contradiction to the present results.

Chen and Chang [50] reported band gap values ranging from 3.56 to 3.71 eV for CeO_2 nanoparticles synthesized by precipitation method at different calcination temperatures. Maensiri et al. [51] presented band gap values ranging from 3.67 to 3.61 eV for CeO_2 synthesized by the sol–gel method using egg white. Similarly, Masui et al. [52] reported band gap values of undoped CeO_2 prepared using reverse micelles to be 3.44 eV.

However, the optical band gap value determined (3.48 eV) was in the range of other reports [53–55]. The explanation of high band gap value is the result of quantum

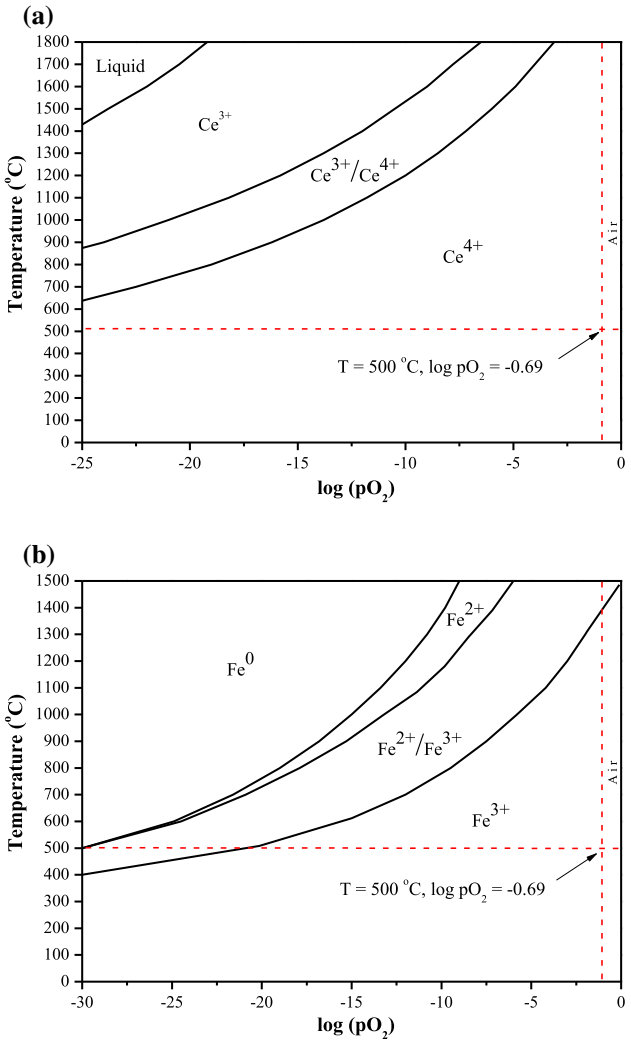

Fig. 5 Calculated thermal stability diagrams of **a** Ce–O and **b** Fe–O

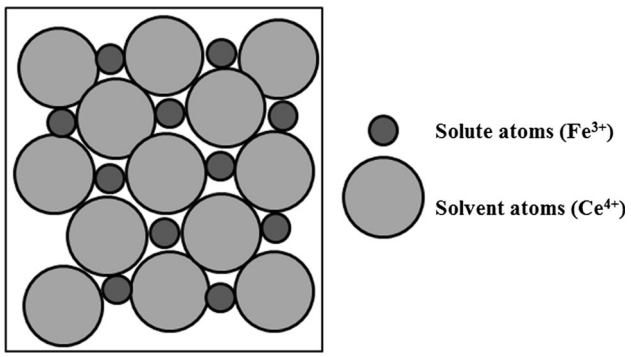

Fig. 6 Schematic illustrating the formation of interstitial solid solution by Fe^{3+} in CeO_2 lattice

confinement effect. Ansari [55] stated that the valence state of the Ce ion following charge transfer and also due to the quantum size effect by decreasing the crystallite size.

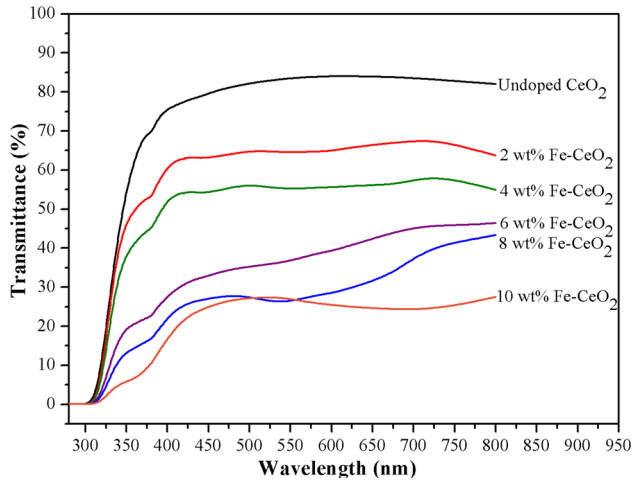

Fig. 7 UV–visible spectra of undoped and Fe-doped CeO_2 films

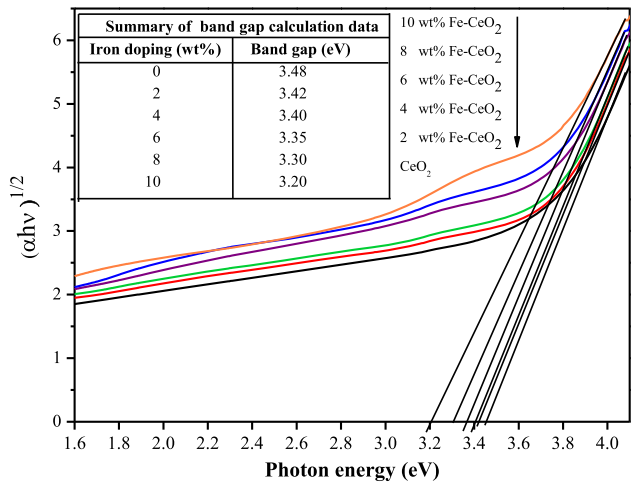

Fig. 8 Optical indirect band gap data for undoped and Fe-doped CeO_2 films

Based on the results, it can be concluded that incorporation of Fe^{3+} ions into the CeO_2 lattice either by shallow electron trapping or by shallow hole trapping would reduce the potential for electron–hole recombination [56–58]. The proposed band structure of undoped CeO_2 and 10 wt% Fe-doped CeO_2 is shown in Fig. 9. Since Fe^{3+} is known to create shallow trapping sites at the donor and acceptor levels, Fe^{3+} doping may decrease the band gap by electron trapping process owing to the substitution of Ce^{4+} or O^{2-} ions by Fe^{3+} ions, and/or by hole trapping in the case of interstitial presence of Fe^{3+} ions in the CeO_2 lattice. Additionally, the increase in the amount of Fe^{3+} dopant can be effective in decreasing the band gap of CeO_2 which would enhance the range of wavelengths that can be absorbed and increase the lifetime of electron–hole separation.

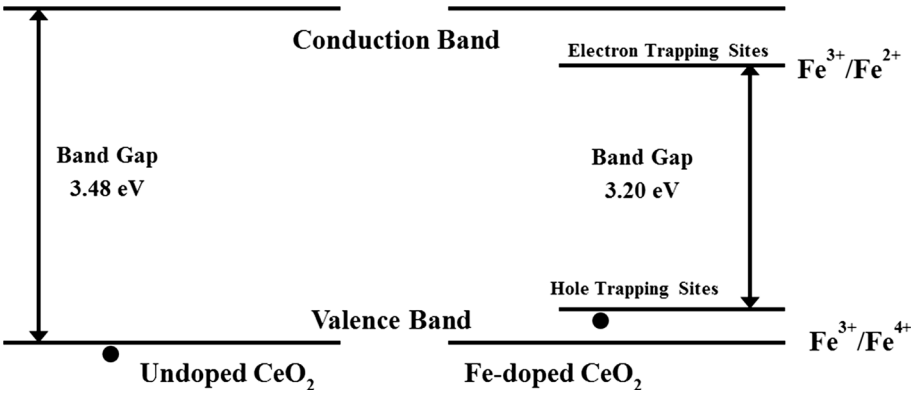

Fig. 9 Hypothetical band structure of undoped CeO_2 and 10 wt% Fe-doped CeO_2

4 Conclusions

Fe-doped CeO_2 thin films have been deposited on FTO-coated glass substrates by spin coating of sol–gel precursors followed by annealing at 500 °C for 5 h. It is important to note that the valence state of Fe^{3+} plays a great role in the mechanism related to solid solution and electron–hole trapping. The thermal stability diagrams suggest that the doped Fe ions exist mainly in the form of Fe^{3+}. The mineralogical data showed that doping CeO_2 with Fe^{3+} resulted in a significant lowering of the transmission of the films in the visible range, although this could be attributed to increased absorption/reflection from the films due to the associated change in color of the films. The decrease in crystallinity of the films with increased dopant concentration is attributed to precipitation of the dopants on the grain boundary which would hinder the recrystallization of CeO_2. This decreased crystallinity could also explain the lowering of transmission due to increased scattering from the amorphous structure.

Based on the proposed band structure, it was concluded that the Fe^{3+} dopant introduced impurity levels that acted as shallow electron−hole trapping inside the band structure of CeO_2, leading to a narrowing of the band gap. This resulted in the Fe-doped films displaying a redshift of the optical absorption edge as well as a lowering of the band gap from 3.48 eV for the undoped CeO_2 films to 3.20 eV to the film with 10 wt% Fe dopant.

Acknowledgments This work has been supported by research funding from Naresuan University (Project No. R2559C001). The authors would like to acknowledge the UNSW node of the Australian Microscopy and Microanalysis Research Facility (AMMRF) for the use of their facilities for the analytical work. The authors acknowledge the Materials Science Research Center, Faculty of Science, Chiang Mai University for providing assistance.

References

1. Martınez-Arias A, Hungrıa AB, Fernandez-Garcıa M, Conesa JC, Munuera G (2004) Interfacial redox processes under CO/O_2 in a nanoceria-supported copper oxide catalyst. J Phys Chem B 108:17983–17991
2. Lin SS, Chang DJ, Wang CH, Chen CC (2003) Catalytic wet air oxidation of phenol by CeO_2 catalyst-effect of reaction conditions. Water Res 37:793–800
3. Tok AIY, Luo LH, Boey FYC, Woodhead JL (2006) Consolidation and properties of $Gd_{0.1}Ce_{0.9}O_{1.95}$ nanoparticles for solid-oxide fuel cell electrolytes. J Mater Res 21:119–124
4. Inoue T, Osonoe M, Tohda H, Hiramatsu M (1991) Low temperature epitaxial growth of cerium dioxide layers on silicon. J Appl Phys 69:8313–8315
5. Kaspar J, Fornasiero P, Graziani M (1999) Use of CeO_2-based oxides in the three-way catalysis. Catal Today 50:285–298
6. Debnath S, Islam MR, Khan MRS (2007) Optical properties of CeO_2 thin films. Bull Mater Sci 30:315–319
7. Misra D, Bauza D, Chen Z, Chikyow T, Iwai H, Obeng Y (2010) CeO_2 optical properties and electrical characteristics. ECS Trans 28:435–442
8. Mills A, Hunte SL (1997) An overview of semiconductor photocatalysis. J Photochem Photobiol A 108:1–35
9. Liqiang J, Xiaojun S, Jing S, Weimin C, Zili X, Yaoguo D, Honggang F (2003) Review of surface photovoltage spectra of nanosized semiconductor and its applications in heterogeneous photocatalysis. Sol Energy Mater Sol Cells 79:133–151
10. Channei D, Inceesungvorn B, Wetchakun N, Ukritnukun S, Nattestad A, Chen J, Phanichphant S (2014) Photocatalytic degradation of methyl orange by CeO_2 and Fe-doped CeO_2 films under visible light irradiation. Sci Rep 4:1–7
11. Isono R, Yoshimura T, Esumi K (2005) Preparation of Au/TiO_2 nanocomposites and their catalytic activity for DPPH radical scavenging reaction. J Colloid Interface Sci 288:177–183
12. Choi W, Termin A, Hoffmann MR (1994) Role of metal-ion dopants in quantum-recombination dynamics. J Phys Chem 98:13669–13679
13. Usseglio S, Damin S, Scarano D, Bordiga S, Zecchina A, Lamberti C (2007) $(I_2)_n$ encapsulation inside TiO_2: a way to tune photoactivity in the visible region. J Am Chem Soc 129:2822–2828
14. Avila-Paredes HJ, Jain P, Sen S, Kim S (2010) Oxygen transport in Sc-doped CeO_2: cation (45Sc) NMR as a probe of anionic conductivity. Chem Mater 22:893–897
15. Dutta G, Saha SK, Waghmare UV (2010) Effects of Zr and Ti doping on the dielectric response of CeO_2: a comparative first-principles study. Solid State Commun 150:2020–2022
16. Santos EL, Muccillo R, Muccillo ENS (2008) Densification and electrical conductivity of Mn-doped CeO_2. Mater Sci Forum 591–593:639–643
17. Wen QY, Zhang HW, Yang QH, Li S, Xu DG, Yao JQ (2009) Fe-doped polycrystalline CeO_2 as terahertz optical material. Chin Chem 26:047803–047807

18. Kumar S, Kim YJ, Koo BH, Choi H, Lee CG (2009) Structural and magnetic properties of Co doped CeO_2 nanoparticles. IEEE Trans Magn 45:2439–2441
19. Kumar S, Kim YJ, Koo BH, Lee CG (2010) Structural and magnetic properties of Ni doped CeO_2 nanoparticles. J Nanosci Nanotechnol 10:7204–7207
20. Neiva LS, Leal E, Melo Costa ACF, Mascarenhas AJS, Andrade HMC, Gama L (2010) Evaluation of the Cu dopping effects in CeO_2 catalytic supports obtained by combustion reaction. Mater Sci Forum 660:899–903
21. Huang J, Yang L, Mao Z (2007) Advanced hybrid ion conducting ceramic composites and applications in new fuel cell generation. Key Eng Mater 336–338:413–418
22. Abe T, Suzuki E, Nagoshi K, Miyashita K, Kaneko M (1999) Electron source in photoinduced hydrogen production on Pt-supported TiO_2 particles. J Phys Chem B 103:1119–1123
23. Subramanian V, Wolf EE, Kamat PV (2003) Green emission to probe photoinduced charging events in ZnO–Au nanoparticles: charge distribution and fermi-level equilibration. J Phys Chem B 105:7479–7485
24. Teoh WY, Madler L, Beydoun D, Pratsinis SE, Amal R (2005) Direct (one-step) synthesis of TiO_2 and Pt/TiO_2 nanoparticles for photocatalytic mineralisation of sucrose. Chem Eng Sci 60:5852–5861
25. Cossarutto L, Chaoui N, Millon E, Muller JF, Lambert J, Alnot M (1998) CeO_2 thin films on Si (100) obtained by pulsed laser deposition. Appl Surf Sci 126:352–355
26. Becht M, Morishiata T (1996) Thin film growth and microstructure analysis of CeO_2 prepared by MOCVD. Chem Vap Depos 2:191–197
27. Zheng SY, Andersson-Faldt AM, Stjerna B, Granqvist CG (1993) Optical properties of sputter-deposited cerium oxyfluoride thin films. Appl Opt 32:6303–6309
28. Azens A, Kullman L, Ragan DD, Granqvist CG (1998) Optically passive counter electrodes for electrochromic devices: trans metal-cerium oxide thin films. Sol Energy Mater Sol Cells 54:85–91
29. Djanovski G, Beshkova M, Velinova S, Mollov D, Vlaev P, Kovacheva D, Vutova K, Mladenov G (2006) Deposition of CeO_2 films on Si(100) substrates by electron beam evaporation. Plasma Process Polym 3:197–200
30. Elidrissi B, Addou M, Regragui M, Monty C, Bougrine A, Kachouane A (2000) Structural and optical properties of CeO_2 thin films prepared by spray pyrolysis. Thin Solid Films 379:23–27
31. Kozjek Skofic I, Sturm S, Ceh M, Bukovec N (2002) CeO_2 thin films obtained by sol–gel deposition and annealed in air or argon. Thin Solid Films 422:170–175
32. Kwak DJ, Moon BH, Lee DK, Park CS, Sung YM (2001) Comparison of transparent conductive indium tin oxide, titanium-doped indium oxide, and fluorine-doped tin oxide films for dye-sensitized solar cell application. J Electr Eng 6:684–687
33. Yang JH, Bark CW, Kim KH, Choi HW (2014) Characteristics of the dye-sensitized solar cells using TiO_2 nanotubes treated with $TiCl_4$. Materials 7:3522–3532
34. Petrova NL, Todorovska RV, Todorovsky DS (2006) Spray-pyrolysis deposition of CeO_2 thin films using citric or tartaric complexes as starting materials. Solid State Ion 177:613–621
35. Tauc J, Menth A (1972) States in the gap. J Non-Cryst Solids 8–10:569–585
36. Mitsunaga T (2009) X-ray thin-film measurement technique. Rigaku J 25:7–12
37. Nakaruk A, Ragazzon D, Sorrell CC (2010) Anatase–rutile transformation through high-temperature annealing of titania films produced by ultrasonic spray pyrolysis. Thin Solid Films 518:3735–3742
38. Khare A, Choudhary RJ, Bapna K, Phase DM, Sanyal SP (2010) Resonance photoemission studies of (111) oriented CeO_2 thin film grown on Si (100) substrate by pulsed laser deposition. J Appl Phys 108:1–5
39. Sharma SK, Knobel M, Meneses CT (2009) Ferromagnetic properties of bulk Fe-doped CeO_2 dilute magnetic semiconductors. J Korean Phys Soc 55:1018–1021
40. Tomaszewski H, Eufinger K, Poelman H, Poelman D, Gryse RD, Marin GB (2007) Effect of substrate sodium content on crystallization and photocatalytic activity of TiO_2 films prepared by DC magnetron sputtering. Int J Photoenergy 95213:1–5
41. Ragazzon D, Nakaruk A, Sorrell CC (2010) Deposition rate of anatase films by ultrasonic spray pyrolysis. Adv Appl Ceram 109:196–199
42. Tan YN, Wong CL, Mohamed AR (2011) An overview on the photocatalytic activity of nano-doped-TiO_2 in the degradation of organic pollutants. ISRN Mater Sci 2011:1–19
43. Shannon RD (1976) Revised effective ionic radii and systematic studies of interatomie distances in halides and chaleogenides. Acta Crystallogr A 32:751–767
44. Salaken SM, Farzana E, Podder J (2013) Effect of Fe-doping on the structural and optical properties of ZnO thin films prepared by spray pyrolysis. J Semicond 34:073003(1)–073003(6)
45. Chen ZC, Zhuge LJ (2007) Initial study on the structure and optical properties of $Zn_{1-x}Fe_xO$ films. Thin Solid Films 515:5462–5465
46. Elidrissi B, Addou M, Regragui M, Monty C, Bougrine A, Kachouane A (2000) Structural and optical properties of CeO_2 thin films prepared by spray pyrolysis. Thin Solid Films 379:23–27
47. Janicki V, Zorc H (2002) Refractive index profiling of CeO_2 thin films using reverse engineering methods. Thin Solid Films 413:198–202
48. Stefanov P, Tanasova G, Stoychev D (2004) Electrochemical deposition of CeO_2 on ZrO_2 and Al_2O_3 thin films formed on stainless steel. Surf Coat Technol 180:446–449
49. Logothetidis S, Patsalas P, Evangelou EK, Konofaos N, Tsiaoussis I, Frangis N (2004) Dielectric properties and electronic transitions of porous and nanostructured cerium oxide films. Mater Sci Eng B 109:69–73
50. Chen HI, Chang HY (2005) Synthesis of nanocrystalline cerium oxide particles by the precipitation method. Ceram Int 31:795–802
51. Maensiri S, Marsingboon C, Loakul P, Jareonboon W, Promarak V, Anderson PL, Seraphin S (2007) Egg white synthesis and photoluminescence of platelike clusters of CeO_2 nanoparticles. Cryst Growth Des 7:950–955
52. Masui T, Fujiwara K, Machida K, Adachi G, Sakata T, Mori H (1997) Characterization of cerium(IV) oxide ultrafine particles prepared using reversed micelles. Chem Mater 9:2197–2204
53. Debnath S, Islam MR, Khan MSR (2007) Optical properties of CeO_2 thin films. Bull Mater Sci 30:315–319
54. Zhang YW, Si R, Liao CS (2003) Facile alcohothermal synthesis, size-dependent ultraviolet adsorption, and enhanced CO conversion activity of ceria nanocrystals. J Phys Chem B 107:10159–10167
55. Ansari AA (2010) Optical and structural properties of sol–gel derived nanostructured CeO_2 film. J Semicond 31:053001(1)–053001(5)
56. Nowotny J, Sorrell CC, Sheppard LR, Bak T (2005) Solar-hydrogen: environmentally safe fuel for the future. Int J Hydrog Energy 30:521–544
57. Cong Y, Zhang J, Chen F, Anpo M, He D (2007) Preparation, photocatalytic activity, and mechanism of Nano-TiO_2 Co-doped with nitrogen and iron (III). J Phys Chem C 111:10618–10623
58. Ke SC, Wang TC, Wong MS, Gopal NO (2006) Low temperature kinetics and energetics of the electron and hole traps in irradiated TiO_2 nanoparticles as revealed by EPR spectroscopy. J Phys Chem B 110:11628–11634